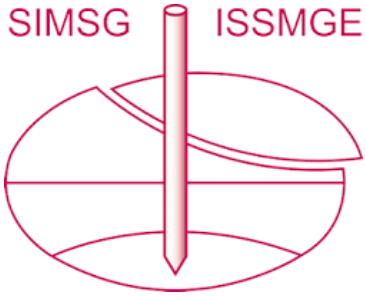
INTERNATIONAL SOCIETY FOR
SOIL MECHANICS AND
GEOTECHNICAL ENGINEERING



This paper was downloaded from the Online Library of the International Society for Soil Mechanics and Geotechnical Engineering (ISSMGE). The library is available here:

https://www.issmge.org/publications/online-library

This is an open-access database that archives thousands of papers published under the Auspices of the ISSMGE and maintained by the Innovation and Development Committee of ISSMGE.

The paper was published in the proceedings of the 6th International Conference on Geotechnical and Geophysical Site Characterization and was edited by Tamás Huszák, András Mahler and Edina Koch. The conference was originally scheduled to be held in Budapest, Hungary in 2020, but due to the COVID-19 pandemic, it was held online from September 26th to September 29th 2021.

Accounting for stress-dependent stiffness of skirted circular foundation during monotonic loading in layered seabed

A. Barari
Department of Civil Engineering, Aalborg University, 9220 Aalborg Ø, Denmark, email: ab@civil.aau.dk

L.B.Ibsen
Department of Civil Engineering, Aalborg University, 9220 Aalborg Ø, Denmark, e-mail: lbi@civil.aau.dk

ABSTRACT: Calibration of Hardening Soil Model with Small-Strain Stiffness (HSsmall) for the centrifuge test of a laterally loaded suction caisson on a natural deposit of Yellow sea silty sand underlain by sandy silt is presented. The HSsmall model, in principle, consists of shear and compression hardening and is capable of simulating the stress-dependency of soil stiffness. A study site off the coast of Korea, so called Yellow sea, was selected as the reference prototype site which is considered to have great potential for future offshore wind farms. The study site seabed is composed of three layers of soil, of which only the top two layers are of interest. The top soil consists of a dense silty sand classified as SM and extends from the ground level to 11 m of depth. The second soil layer consists of a thick sandy silt from 11 m to 32 m of depth. Monotonic centrifuge test was performed on suction caisson having 15.5 m diameter and 10.5 m skirt length. Calibration of the HSsmall model was based on monotonic test data, drained triaxial tests, shear wave velocity measurements, CPT test data and empirical relationships for shear modulus at small strains.

Keywords: calibration; suction bucket; HSsmall; centrifuge; stiffness

1. Introduction

Several foundation types exist for offshore wind turbines, and the choice of foundation type depends on many factors such as water depth, soil conditions, climate, seismic activity etc. In 2015, about 80% of all offshore wind turbines in Europe were installed on monopile foundations [1]. Installation of monopiles are carried out by driving it into the seabed by hammering. The construction of a monopile is cost efficient but the installation is time consuming and not very environmentally friendly. A promising new foundation type for offshore wind turbines is the suction bucket concept due to its many advantages in the offshore environment: 1) It can be towed to site and installed in the seabed by creating an under pressure in the bucket, removing the need for any hammering equipment, resulting in an environmental friendly and noise free installation, 2) by controlling the suction during installation it can be self levelling, removing the need for a transition piece to adjust for verticality, and 3) after operational use it can be removed by a reverse pressuring procedure, leaving the seabed intact.

Offshore wind turbines are subjected to four main loading types: wind and wave loads [2], and 1P and 3P loads. 1P loading is caused by mass and aerodynamic imbalances of the rotor whose forcing frequency equals the rotational frequency of the rotor. 3P loading is induced in the tower due to the vibrations of the blade shadowing effect [3]. In addition, less frequent loads such as seismic and ice loads can also be of great importance for the design of offshore wind turbines, although these loads are more regionally dependent [4-6]. All loads have unique characteristics in terms of magnitude, frequency and number of applied load cycles.

The required design limit states are represented in the standard Design of Offshore Wind Turbine Structures from Det Norske Veritas [7]:

(1) *Ultimate limit state (ULS)*: refers to the ultimate bearing capacity of the foundation when subjected to all possible design load cases. The ultimate limit state is also reached by loss of structural resistance, failure of components and loss of static equilibrium
(2) *Fatigue limit state (FLS):* refers to failure in structural elements due to long-term effects from cyclic loading.
(3) *Accidental limit state (ALS):* refers to failure in structural damage caused by accidental loads.
(4) Serviceability limit state (SLS): refers to the state at which deformations and settlements of the foundation exceeds the tolerance level. For instance, the maximum allowed rotational tilt of an offshore wind turbine are typically set to 0.5°.

1.1. Problem Statement

The problem of bearing capacity under general loading has been of particular interest in the field of offshore renewable energy and previous relevant studies have been confined to laboratory model tests [8-11], field tests [12] and numerical studies [13-16].

Investigation of the bearing capacity of shallow foundations has particularly considered work-hardening plasticity theory (e.g., [13] and [17-19]). The developed theories provide a suitable simulation of the load-deformation response of shallow footings.

Yet applicability of the observations in laboratory tests at 1g (i.e, acceleration field identical to the acceleration of gravity) to soil-structure system has remained uncertain. The cohesionless soil exhibits dilatancy at low stress

levels, which may not take place in the field [20]. However, the collected data reported in LeBlanc et al. [21] also confirmed the likelihood of higher peak friction angle than soil with identical relative density present in the field.

This paper is devoted to presenting the results from numerical analyses using HSsmall constitutive soil model to simulate the nonlinear interaction of suction bucket foundation for offshore wind turbines. As the behavior of soil elements/1g lab tests cannot be directly transferred to the earth systems [22], the calibration of the HSsmall model against element tests is adopted by means of well-documented centrifuge tests of monobucket configuration in sand [23]. The insights gained from the numerical analyses will be utilized to provide guidance on the detailed guidance on the detailed design of a foundation system.

2. Centrifuge test description

The centrifuge tests were carried out at a centrifugal acceleration of 70g. The soil model and soil specimen were installed in a cylindrical rigid container made of steel, measuring 900 mm in diameter and 700 mm in depth, equivalent to prototype dimensions of 63 m in diameter and 49 m of depth.

2.1. Prototype seabed conditions

A study site off the coast of Korea was selected as the reference prototype site, as this location called the Yellow sea, is considered to have great potential for future offshore wind farms. The seabed here is composed of silty sand and sandy silt sediments and the water depth is 15 m. The study site seabed is composed of three layers of soil, of which only the top two layers are of interest, denoted here the top and bottom soil.

The top soil consists of a silty sand and extends from the ground level to 11 of depth. The second soil layer consists of a thick sandy silt from 11 m to 32 m of depth. The two soils have been classified as SM and ML in the united classification soil system (USCS), respectively.

2.2. Model configuration

The foundation configuration in the centrifuge test is shown in Fig. 1. The model dimensions were chosen by scaling down the prototype dimensions of the monopod dimension at a scale of 1:70 according to the centrifuge scaling laws. However, to avoid structural deformation of the skirt and lid of the buckets, the thickness of these were upscaled to 1 and 3 mm respectively. The final modeled specifications of the centrifuge models compared to the prototype models are shown in Table 1. The resulting conditions achieved are displayed in Table 2.

Table 1. Specifications of prototype and model bucket foundations [23]

Item	Dimension	
	Prototype (m)	Model (mm)
Bucket diameter, D	15.5	221.4
Skirt length, L	10.5(0.68D)	150(0.68D)
Skirt thickness	0.04(0.26%D)	1(0.45%D)
Top lid thickness	0.04(0.26%D)	7(3.15%D)
Weight	4.49 MN	---

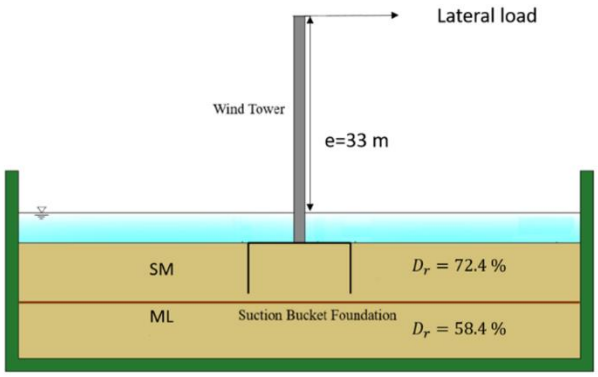


Figure 1. Overview of the centrifuge model used in the numerical analyses

Table 2. Conditions of centrifuge soil specimen [23]

Test	Type	$\gamma_d(t/m^3)$		$D_r(\%)$		Loading
		SM	ML	SM	ML	
T1	Mono-bucket	1.5	1.44	72.4	58.4	Monotonic

Prior to the loading tests, a miniature cone penetration test (CPT) and shear wave velocity measurements were conducted to characterize the model seabed at 70g. The CPT data and shear wave velocity measurements are shown in Fig. 2.

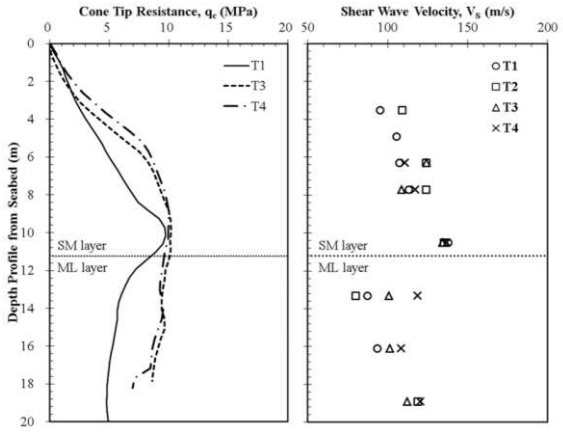


Figure 2. Cone tip resistance and shear wave velocity profiles [24]

3. Numerical modeling: general assumptions

The FE analyses are conducted in PLAXIS 3D. However, due to axisymmetry, the monopod is reduced to half size as shown in Fig.3, which reduces computational costs significantly.

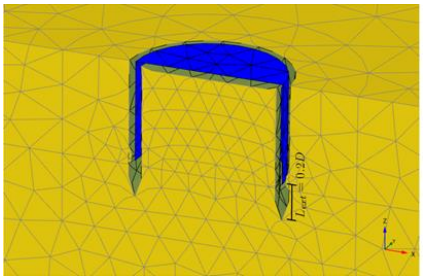


Figure 3. Axisymmetric geometry of monopod with extended interfaces.

Interfaces: To model a realistic soil-structure interaction, interfaces can be created along the contact surfaces between the structure and the soil. However, stress concentrations can arise at the corners of stiff structures such as bucket skirt due to abrupt changes in geometry. This may lead to numerical instabilities and an unrealistic weakening of the soil. This problem can be solved by the use of extended interfaces. Therefore extended vertical interfaces of length , $L_{ext} = 0.2D$ are introduced at the tip of the bucket, see Fig. 3, as suggested by Østergaard et al. [35]. R_{inter} defines the interface strength reduction factor for the interface between the structure and the surrounding soil. For a realistic soil-structure interaction, the interface will be weaker and more flexible than the surrounding soil, this is why it should have a value less than 1. The interface strength is defined as in Eq. (1).

$$R_{inter} = tan\delta/tan\varphi \quad (1)$$

where $\delta = k.\varphi$, in which k is the interface strength reduction coefficient. Kim et al. [23] found that the interaction between the steel bucket and the upper layer of sand was found with k=2/3 measured by 1-g shear tests, and is therefore implemented in FE model. It should however be noted that the reduced strength properties corresponding to extended interfaces are not intended for soil-structure interaction analysis. Hence, the strength of these interfaces should set as rigid i.e. $R_{inter} = 1$.

Steel Material: This study investigates the behavior of the surrounding soil and not the internal forces within the structure. Therefore, the skirt and lid steel material is modeled with an unrealistic high Young's modulus of 180000 MPa and a plate thickness of 0.2 m, thus simulating a rigid body response. This ensures no deflection of the bucket itself and the soil-structure behavior can then be interpreted in more detail.

Boundary conditions and staged construction: The aim of the numerical modeling is to replicate the centrifuge tests, which are conducted within a cylindrical steel container. Therefore, the boundary conditions are chosen as follows:

A set of fixities are applied to all directions at the bottom, in both horizontal directions on the periphery and in the direction normal to the plane on the symmetry plane. The FEM analyses are conducted in in several calculation stages. In the initial step, geostatic stresses in the model consisting of soil elements were calculated by application of gravity loading. In this case, the lateral earth pressure coefficient at rest, K_0, is calculated by Jaky's formulation: $K_0 = 1 - sin(\varphi')$ [36]. Subsequently, the predefined elements defining the bucket geometry were replaced by steel elements modeling the bucket structure. Afterwards, static pushover analyses were performed for given structural configuration.

4. Calibration of HSsmall model

Hardening soil model with small-strain stiffness (HSsmall) is basically based on the original Hardening soil model (HS). One of the key features of the HS model, as opposed to the Mohr-Coulomb model, is that it takes into account soil hardening during plastic loading, which is assumed to capture real soil behavior more accurately. This means that while the Mohr-Coulomb model assumes a fixed yield surface, the yield surface of the HS model is allowed to expand. To do this, the HS model incorporates an isotropic hardening law, which means the size of the yield loci can increase while the position and shape of the yield loci remains the same. The HS model also uses three different input stiffnesses; the triaxial secant modulus, E_{50}, the unloading/reloading stiffness modulus, E_{50}, E_{ur}, and the oedometer stiffness modulus, E_{oed}, as well as accounting for stress-dependency of stiffness moduli. In addition, the HSsmall model accounts for the variation of shear stiffness at very small strains. The soil parameters required as input for the HSsmall model are presented in Table 3.

Table 3. Input parameters for HSsmall model [26]

Strength parameters	Symbol	Unit
Effective cohesion	C'	kPa
Effective friction angle	φ'	[°]
Dilatancy angle	ψ'	[°]
Tension cut-off and tensile Strength	σ_t	kPa
Stiffness parameters		
Secant stiffness in drained Triaxial test	E_{50}^{ref}	kPa
Oedometer stiffness	E_{oed}^{ref}	kPa
Unloading/reloading stiffness	E_{ur}^{ref}	kPa
Power for stress-level dependency of stiffness	m	-
Small strain shear modulus	G_0^{ref}	kPa
Threshold shear strain	$\gamma_{0.7}$	-
Advanced parameters		
Reference pressure	p^{ref}	kPa
Lateral earth pressure coefficient at rest	K_0	-
Failure ratio q_f/q_a	R_f	-

The soil parameters for the two soil layers, SM and ML, can be estimated from the provided soil conditions presented in Table 2 and from the CPT data presented in Fig.2. However, additional soil data exist from the SM layer, which are presented in the Kim et al. [24]. This additional data consist of multiple triaxial shear tests conducted on the SM layer, which allow for more sophisticated determination of the strength and stiffness parameters than those estimated from a CPT test. This also entails that a more advanced constitutive soil model can be used to describe the behavior of SM layer in a FE analysis. In this case, the HSsmall model have been utilized for the SM layer.

The only available soil data for the ML layer is the soil conditions in the centrifuge tests, presented in Table 2, and the CPT data presented in Fig. 2.

4.1. Input parameters: SM layer

4.1.1. Strength parameters φ', ψ and c'

The basic soil conditions of the SM layer in test T1 are presented in Table 4. These data originate partly from the [23] and [24].

Table 4. Soil conditions of SM layer in test T1

Parameter	Symbol	Value	Unit
Fines content	P#200	47	%
Grain size	d_{10}	0.045	mm
	d_{50}	0.08	mm
	d_{60}	0.095	mm
Coefficient of uniformity	C_u	2.11	-
Relative density	D_r	72.4	%
Dry density	ρ_d	1.5	t/m^3
Specific gravity	G_s	2.67	-
Void ratio	e	0.78	-
Unsaturated unit weight	γ_d	14.72	kN/m^2
Saturated unit weight	γ_{sat}	19.01	kN/m^2

The strength parameters are determined based on the findings of Kim et al. [24]. The effective friction angle,φ', has been determined by linear interpolation to match a relative density of 72.4%. The dilatancy angle, ψ, is determined from the drained triaxial tests according to Eq. (2) [25]:

$$\psi = arcsin\left(\frac{\frac{d\varepsilon_v}{d\varepsilon_a}}{\frac{d\varepsilon_v}{d\varepsilon_a} - 2}\right) \quad (2)$$

The linear regression components are extracted from the linear fit and the dilatancy angle as a function of relative density is expressed as:

$$\psi = 0.6160 D_r - 33.8716 \quad (3)$$

The dilatancy angle can then be found for the relative density in test T1 of $D_r = 72.4\%$, using the established regression in Eq. (3), which results in an angle of $\psi = 10.7$. This corresponds well with the often used relation: $\psi = \varphi' - 30^{\circ}$ which yields a dilatancy angle of $\psi = 9.2$. The effectiove cohesion, c' , is assumed equal to zero due to the low undrained strength, c_u. However, to avoid numerical instabilities, it is suggested to use a value of at least c' =0.2 kPa [26]. The strength parameters are summarized in Table 5.

Table 5. Strength parameters of SM layer in test T1

Parameter	Symbol	Value	Unit
Effective friction angle	φ'	39.2	[°]
Dilatancy angle	Ψ	10.7	[°]
Cohesion	c_u	2.1	kPa
Effective cohesion	c'	0.2	kPa

4.1.2. Lateral earth pressure coefficient at rest, K_0 and effective poisson's ratio, υ'

The lateral earth pressure coefficient at rest is determined by Jaky's formula for normally consolidated soils [36]:

$$K_0 = 1 - sin\varphi' \quad (4)$$

The effective Poisson's ratio is determined as [27]:

$$\upsilon = \frac{1 - sin\varphi'}{2 - sin\varphi'} \quad (5)$$

4.1.3. Secant stiffness modulus, E_{50} and E_{50}^{ref}

The triaxial data has been used to determine the secant stiffness modulus, E_{50}, which is the secant stiffness at 50% of the maximum deviatoric stress. Fig.4a shows the deviatoric stress with axial strain for three different relative densities. The maximum deviatoric stresses and the corresponding 50% stresses are plotted with dashed lines. The secant moduli are then defined as the slopes of the lines going from origo to the point where the dashed lines intercept the test data. The secant stiffness moduli are then plotted together with the corresponding relative density in Figure 4b. A linear fit of the data is made in order to determine the secant stiffness modulus at a relative density of 72.4%, which is the relative density in test T1.

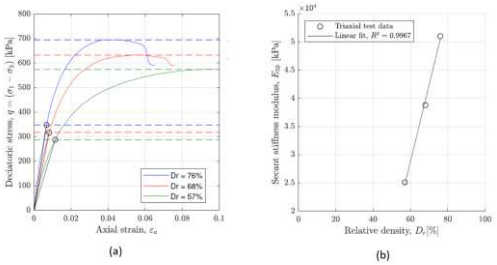


Figure 4. Drained triaxial compression tests on SM sand with varying density. (a) Deviatoric stress with axial strain (b) secant stiffness modulus with relative density

The linear regression components are extracted from the linear fit and the secant stiffness modulus of test:

$$E_{50} = 1355.8D_r - 52549 \quad (6)$$

where E_{50} and D_r are secant stiffness modulus and relative density, respectively.

A reference secant stiffness modulus, E_{50}^{ref}, is used to account for stress dependency , which is calculated as [26]:

$$E_{50}^{ref} = \frac{E_{50}}{\left(\frac{ccos\varphi + \sigma'_3 sin\varphi}{ccos\varphi + p_{ref} sin\varphi}\right)^m} \quad (7)$$

The stress component, *m*, can be calculated from triaxial tests if data with different confining pressures are available. In this case, the only data that was provided was with confining pressures of 400 kPa. The stress component, *m*, has been reported to vary between 0.5 and 1 [26]. However, as this is the only unknown parameter it will act as fitting parameter when calibrating the response to the centrifuge tests.

4.1.4. Unloading/reloading stiffness modulus, E_{ur}^{ref}

E_{ur}^{ref} is the Young's modulus for unloading and reloading, corresponding to the reference pressure, p^{ref}. In absence of unloading/reloading curves from triaxial tests it can be estimated by [26]:

$$E_{ur}^{ref} = 3.E_{50}^{ref} \quad (8)$$

4.1.5. Oedometer stiffness modulus, E_{oed} and E_{oed}^{ref}

In the HSsmall model, no fixed relation exists between the drained triaxial stiffness, E_{50}, and the oedometer stiffness, E_{oed}.These moduli must therefore be taken into account separately. However, in this case, information about the oedometer stiffness does not exist. As a first guess, the relation presented in Brinkgreve et al. [26] is considered as:

$$E_{50}^{ref} = 1.25E_{oed}^{ref} \quad (9)$$

4.1. 6. Shear modulus at very small strains, G_0 and G_0^{ref}

The shear modulus at small strains is fundamentally affected by three factors [28]:

(a) Void ratio of the specimen
(b) Inter-particle contact stiffness, which will depend upon particle mineralogy, angularity, and roughness, and effective stress
(c) Deformation and flexing within individual particles, which will depend on particle mineralogy and shape

The small strain shear modulus can be determined based on the elasticity theory from the shear wave velocity and soil density:

$$G_0 = \rho v_s^2 \quad (10)$$

As shear wave measurements are not commonly carried out in ground investigation work, many empirical correlations have been formulated to estimate G_0. A first rough estimation of G_0 can be calculated using the relative density, for clean sands [29]:

$$G_0 = 167\sqrt{46D_r^2 + 2.5} \quad (11)$$

A more sophisticated determination of G_0 was formulated by Hardin and Richart [30], which takes in to account the void ratio and grain angularity:

$$G_0 = A\frac{(a-e)^2}{1+e}p^n \quad (12)$$

In which the recommended constants are A=6.9, a=2.17, and n=0.5 for round grains and A=3.2, a=2.97 and n=0.5 for angular grains [33]. Void ratio and reference pressure are denoted by e and p, respectively.

Wichtmann and Triantafyllidis [31] showed that G_0 significantly decreases with increasing coefficient of uniformity $c_u = \frac{d_{60}}{d_{10}}$ of the grain size distribution curve and defined the following correlations of the constants in Eq. (12) expressed by the coefficient of uniformity, C_u:

$$a = 1.94exp(-0.066C_u) \quad (13)$$

$$n = 0.4C_u^{0.18} \quad (14)$$

$$A = 1563 + 3.13C_u^{0.18} \quad (15)$$

Wichtmann et al. [32] further observed that G_0 significantly decreases with increasing non-cohesive fines content. To account for this, the small strain shear modulus as a function of fines content, $G_0(FC) = G_0(FC = 0)f_r(Fc)$, where $G_0(FC = 0)$ is small strain shear modulus for clean sand, see Eqs. (12-15) and $f_r(Fc)$ is a reduction factor depending on fines content.

The reduction factor was observed to be almost constant for fines contents above 10%, thus a bi-linear formulation was proposed as:

$$f_r(FC) = Af(x) = \begin{cases} 1 - 0.043FC, & for\ FC \le 10\% \\ 0.57\ , & for\ FC \ge 10\% \end{cases} \quad (16)$$

Table 6 summarizes the values obtained for G_0 using the presented formulations above.

Table 6. G_0 values from different formulations

Theory	Value	Unit
Shear wave measurements *	24752	kPa
Boulanger et al. [29]	82004	kPa
Hardin and Black [33] round grains	74896	kPa
Hardin and Black [33] angular grains	86222	kPa

Wichtmann and Triantafyllidis [31] clean sand	73687	kPa
Wichtmann and Triantafyllidis [31] fines	42001	kPa

*Average value of G_0 in SM layer

As relationship proposed by Wichtmann et al. [32] is the only formulation for G_0 that accounts for the very high fines content for two layers, this approach will be used as the initial guess for the small strain shear modulus. The stress dependency of the shear modulus is expressed with the power law the same way as the secant and oedometer stiffness moduli, but as the small strain shear modulus is not derived from a specific confining pressure, the reference modulus is set equal to the calculated modulus:

$$G_0^{ref} = G_0 \tag{17}$$

4.1.7. Threshold shear strain, $\gamma_{0.7}$

The threshold shear strain at which the secant shear modulus, G_s, is reduced to about 70% of G_0 is calculated with Eq. (18) [26]:

$$\gamma_{0.7} = \frac{1}{9G_0}\Big(2c'\big(1+cos(2\varphi')\big) - \sigma'_1(1+K_0)sin(2\varphi')\Big) \tag{18}$$

where $\gamma_{0.7}$, G_0 and K_0 are threshold shear strain, small strain shear modulus and lateral earth pressure coefficient at rest, respectively.

4.1.8. HSsmall model parameters for SM layer

Table 7 shows the HSsmall model parameters determined from the triaxial test data and the presented stiffness correlations, while Table 8 shows the stress dependent reference stiffness moduli for different stress exponents used for calibration.

Table 7. HSsmall model parameters from triaxial test data on SM sand

Parameter	Value	Unit
φ'	39.18	°
ψ	10.73	°
C'	0.2	kPa
K_0	0.37	-
υ'	0.27	-
e	0.78	-
E_{50}^*	45613	kPa
E_{oed}^*	36490	kPa
G_0	42002	kPa
$\gamma_{0.7}$	3.56×10^{-4}	-

*At a confining pressure of 400 kPa

Table 8. HSsmall model parameters for calibration

Parameter	Value					
m [-]	0.5	0.6	0.7	0.8	0.9	1
E_{50}^{ref} [kPa]	22829	19878	17308	15070	13122	1142
E_{ur}^{ref} [kPa]	68486	59633	51923	45211	39366	3427
E_{oed}^{ref} [kPa]	18263	15902	13846	12056	10498	914
G_0^{ref} [kPa]	42002	42002	42002	42002	42002	4200

4.2. Input parameters for the HSsmall model: ML layer

The basic soil conditions of the ML layer in test T1 are presented in Table 9.

Table 9. Soil conditions of ML layer in test T1

Parameter	Symbol	Value	Unit
Fines content	P#200	75	%
Grain size	d_{10}	0.0055	mm
	d_{50}	0.050	mm
	d_{60}	0.060	mm
Coefficient of uniformity	C_u	10.9	-
Relative density	D_r	58.4	%
Dry density	ρ_d	1.44	t/m^3
Specific gravity	G_s	2.64	-
Void ratio	e	0.83	-
Unsaturated unit weight	γ_d	14.13	kN/m^3
Saturated unit weight	γ_{sat}	18.75	kN/m^3
Cohesion	c_u	10.91	kPa

Due to lack of laboratory test data on the ML layer, friction angle has been determined based on a typical value for silty soils. The dilatancy angle, ψ, is determined as $\psi = \varphi' - 30^\circ$. As for the SM layer, the effective cohesion is set equal to c'=0.2 kPa. The strength parameters are summarized in Table 10.

Table 10. Strength parameters of ML layer

Parameter	Symbol	Value	Unit
Effective friction angle	φ'	30	[°]
Dilatancy angle	ψ	0	[°]

Cohesion	c_u	10.91	kPa
Effective cohesion	C'	0.2	kPa

5. Numerical analyses for T1 test: explicit soil strata

In the absence of sufficient soil data, the strategy hereafter is to model the ML layer by using the more convenient model, so called Mohr-Coulomb, which requires the lowest amount of input parameters. By doing so, only two stiffness parameters are necessary to determine, namely the Young's modulus, E, and the Poisson's ratio, υ. Young's modulus is calculated by Eq. (19) according to Hooke's law:

$$E = \frac{(1-2\upsilon)(1+\upsilon).E_{oed}}{(1-\upsilon)} \quad (19)$$

where the Poisson's ratio, υ, is determined by the friction angle according to Eq. (5), and the oedometer modulus, E_{oed}, is determined baed on CPT correlations. Although stiffness parameters determined from CPT data show low reliability, it has been deemed the only way of obtaining the stiffness as opposed to using typical values proposed in the literature. The oedometer modulus is estimated from CPT cone resistance by Lunne et al. [34]:

$$E_{oed} = \alpha_m . q_c \quad (20)$$

where E_{oed} , α_m and q_c are oedometer stiffness modulus, constant ($3 \leq \alpha_m \leq 6$ $for\ silt$) and q_c is cone resistance.

E_{oed} is calculated with $\alpha_m = 3$ (lower bound) and the obtained values are shown in Fig. 5. To account for the variation of E_{oed} in depth, the ML layer is divided in to three sublayers and an average value is calculated for each sublayer.

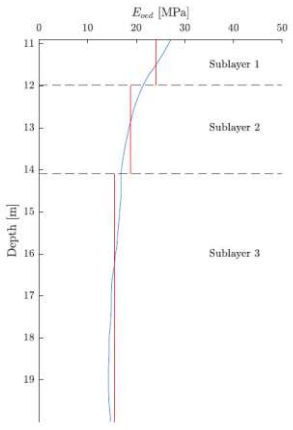


Figure 5. Oedometer stiffness modulus, E_{oed}, from CPT data

The stiffness parameters used to represent the ML layer in this approach are shown in Table 11.

Table 11. Mohr-Coulomb stiffness parameters for ML layer

Parameter	Sublayer 1	Sublayer 2	Sublayer 3
Oedometer modulus, E_{oed} [MPa]	24.06	18.82	15.49
Poisson's ratio, υ [-]	0.33	0.33	0.33
Young's modulus, E [MPa]	16.04	12.54	10.32

The resulting moment, M, is plotted against the rotation of the monopod, see Fig.6, in order to compare the numerical results with the results from the centrifuge test.

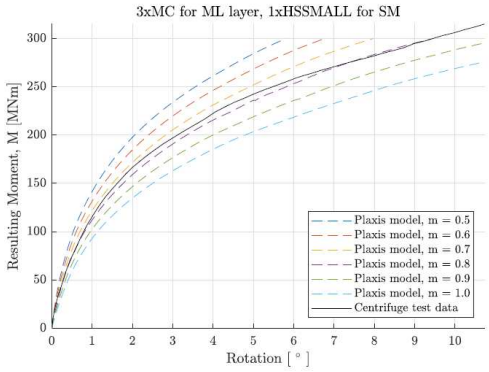


Figure 6. Moment-rotation diagram for varying stress dependency factors, m (ML layers with Mohr-Coulomb model and SM layer with HSsmall model)

As can be seen in Fig.6, the best fit with this approach is achieved with a stress dependency factors between m=0.7-0.8.

6. Conclusions

The ability of numerical model to predict angular rotation of the soil-foundation system in yellow sea seabed as the reference prototype site is investigated.

The Yellow sea offshore site was characterized using cone penetration tests and shear wave velocity measurements, and advanced laboratory testing. Calibration, which was developed for representing SM and ML soils, focused on (1) drained triaxial compression tests and resultant stress-strain responses; (2) stress-dependence of the secant stiffness moduli and equivalent relative densities; and (3) CPT tip resistance and shear wave velocity profiles.

Numerical study was then carried out to capture the caisson load-displacement response given by centrifuge experiment, incorporating the correlations for the stress-dependent secant stiffness and exponent for stress-level dependency for the upper soil layer.

Acknowledgments

The authors gratefully acknowledge the financial support received from the European Union's Horizon 2020 research and innovation program under grant agreement No 818153. This study is funded as part of

i4Offshore project (Integrated Implementation of Industrial Innovations for Offshore Wind Cost Reduction).

References

[1] EWEA. (2015). "The European offshore wind industry- key trends and statistics 2015", http://www.ewea. org/library/statistics/offshore/.

[2] Barari, A., Bagheri, M., Rouainia, M., Ibsen, L.B. "Deformation mechanisms for offshore monopile foundations accounting for cyclic mobility effects", Soil Dynamics and Earthquake Engineering, 97, pp.439-453, 2017.

[3] Bhattacharya, S., Lombardi, D., Nikitas, G. "Physical modeling of offshore wind turbine model for prediction of prototype response", Wind Energy Engineering, pp.353-374, 2017, ISBN:978-0-12-809451-8.

[4] Zheng, X.Y., Li, H., Rong, W. and Li, W. "Joint earthquake and wave action on the monopile wind turbine foundation: An experimental study", Marine Structures, 44, pp.125-141, 2015.

[5] Barari, A., Bayat, M., Saadati, M., Ibsen, L.B. "Transient analysis of monopile foundations partially embedded in liquefied soil". Geomechanics and Geoenginering: An International Journal, 5(2), pp.127-135, 2015.

[6] Wang, X., Yang, X., Zeng, X. "Seismic centrifuge modelling of suction bucket foundation for offshore wind turbine", Renewable Energy, 114, DOI: 10.1016/j.renene.2017.07.103, 2017.

[7] DNV-OS-J101. "DNV-OS-J101 Design of offshore wind turbine structures", 2011.

[8] Ibsen, L.B., Larsen, K.A., Barari, A. "Calibration of failure criteria for bucket foundations on drained sand under general loading", Journal of Geotechnical and Geoenvironmental Engineering, 140 (7), 2014, DOI: 10.1061/(ASCE)GT.1943-5606.0000995.

[9] Ibsen, L.B., Barari, A., Larsen, K.A. "Adaptive plasticity model for bucket foundations", Journal of Engineering Mechanics, 2014, DOI: 10.1061/(ASCE)EM.1943-7889.0000633.

[10] Barari, A., Ibsen, L.B. "Undrained response of bucket foundations to moment loading", Applied Ocean Research, 36, pp.12-21, 2012.

[11] Larsen, K.A., Ibsen, L.B., Barari, A. "Modified expression for the failure criterion of bucket foundations subjected to combined loading", Canadian Geotechnical Journal, 50 (12), pp.1250-1259, 2013.

[12] Burd, H.J., Beuckelaers, W.J.A.P., Byrne, B.W., Gavin, K., Houlsby, G.T., Igoe, D., Jardine, R.J., Martin, C.M., McAdam, R.A., Muir Wood, A., Potts, D.M., Skov Gretlund, J., Taborda, D.M.G., Zdravkovic, L. (2019). "New data analysis methods for instrumented medium scale monopile field tests", Géotechnique, DOI: 10.1680/jgeot.18.pisa.002, 2019.

[13] Gerolymos, N., Zafierakos, A., Souliotis, C. "Lateral response of caisson foundations: A macro-element approach", 15 WCEE, Lisboa 2012, 2012.

[14] Gourvenec, S. "Effect of embedment on the undrained capacity of shallow foundations under general loading", Géotechnique, 58(3), pp.177-185, 2008.

[15] Bienen, B., Gaudin, C.H., Cassidy, M., Rausch, L. and Purwana, O. A. "Numerical modeling of undrained capacity of hybrid skirted foundation under combined loading", International Journal of Offshore and Polar Engineering, 22(4), pp.323–329, 2012.

[16] Achmus, M., Akdag, C. T., Thieken, K. "Load-bearing behavior of suction bucket foundations in sand", Applied Ocean Research, 43, pp. 157–165, 2013.

[17] Cassidy, M.J., Byrne, B.W., Houlsby, G.T. "Modelling the behavior of circular footings under combined loading on loose carbonate sand", Géotechnique, 52(10), pp.705–712, 2002.

[18] Gottardi, G., Houlsby, G. T. and Butterfield, R. "Plastic response of circular footings on sand under general planar loading", Géotechnique, 49(4), pp.453–469, 1999.

[19] Byrne, B. W., Houlsby, G. T. "Observations of footing behaviour on loose carbonate sands", Géotechnique, 51(5), pp.463–466, 2001.

[20] Guo, W.D., Qin, H.Y. "Thrust and bending moment of rigid piles subjected to moving soil", Canadian Geotechnical Journal, 47(2), pp.180-196, 2010.

[21] LeBlanc, C., Houlsby, G.T., Byrne, B. "Response of stiff piles in sand to long-term cyclic lateral loading", Géotechnique, 60(2), pp.79-90, 2010.

[22] Cuellar, P., Baeßler, M., Georgi, S., Rücker, W. "Special issues for the coupled transient simulation of laterally loaded offshore piles and novel experimental findings." Workshop "Gründung von Offshore-Windenergieanlagen" (ed. T. Triantafyllidis), Publications of the Institute of Soil Mechanics and Rock Mechanics, Karlsruhe Institute of Technology (KIT), No. 172, 2010.

[23] Kim, D.J., Choo, Y.W., Kim, J.H., Kim, S. "Investigation of monotonic and cyclic behavior of tripod suction bucket foundations for offshore wind towers using centrifuge modeling", Journal of Geotechnical and Geoenvironmental Engineering, 140(5), 2014, DOI: 10.1061/(ASCE)GT.1943-5606.0001083.

[24] Kim, J.H., Choo, Y.W., Kim, J. Kim, D.S. "Miniature Cone Tip Resistance on Sand in a Centrifuge", Journal of Geotechnical and Geoenvironmental Engineering, 142(3), 2014, DOI: 10.1061/(ASCE)GT.1943-5606.0001425.

[25] Maranha, J.R., Neves, M.D. "The experimental determination of the angle of dilatancy in soils", IOS Press, Amsterdam, 2009.

[26] Brinkgreve, R.B.J., Kumarswamy, S., and Swolfs, W.M. (2018). "PLAXIS 3D 2018 Manual". ISBN 13: 978-90-76016-26-9.

[27] DNV GL AS. (2017). "DNVGL-RP-C212 Offshore Soil Mechanics and Geotechnical Engineering".

[28] Clayton, C.R.I. “Stiffness at small strain: research and practice”, Geotechnique, 61, pp.5-37, 2011.
[29] Boulanger, R.W. and Ziotopoulou, K. “PM4SaND (version 3): A sand Plasticity model for earthquake engineering Applications”, pp.1-108, 2015.
[30] Hardin, B. O., Richart, F.E. “Elastic wave velocities in granular soils”, J. Soil Mech. Found. Div., 89(SM2), 1963.
[31] Wichtmann, T. and Triantafyllidis, T. “Influence of the grain-size distribution curve of Quartz sand on the small strain shear modulus G_{max}”, Journal of Geotechnical and Geoenvironmental Engineering,135(19),2009,DOI:10.1061/(ASCE)GT.1943-5606.0000096.
[32] Whitchtmann, T., Navarrete Hernandez, M.A., Triantafyllidis, T. “On the influence of a non-cohesive fines content on small strain stiffness, modulus degradation and damping of quartz sand”, Soil Dynamics and Earthquake Engineering, 69, pp.103-114, 2015.
[33] Hardin, B.O., Black, W.L. “Sand stiffness under various triaxial stresses”, J.Soil Mech. Found. Div., 89(SM2), 1966.
[34] Lunne, T., Robertson, P.K., Powell, J.J.M. “Cone penetration testing in Geotechnical Practice”, Blackie Academic and Professional, London, 1997.
[35] Østergaard, M.U., Knudsen, B.S., Ibsen, L.B. “p-y curves for bucket foundations in sand using finite element modeling”, Frontiers in Offshore Geotechnics III: Proceedings of the Third International symposium in Frontiers in Offshore Geotechnics (ISFOG), Oslo, Norway, pp. 343-348, 2015.
[36]Jaky, J. “The coefficient of earth pressure at rest”, Journal of the Society of Hungarian Architects and Engineering, 78(22), pp. 355-358, 1944.